Experimental study on interfacial and wall friction factors under counter-current flow limitation in vertical pipes with sharp-edged lower ends

Goda, Raito
Hayashi, Kosuke
Murase, Michio
Hosokawa, Shigeo
Tomiyama, Akio

(Citation)
Nuclear Engineering and Design,353:110223

(Issue Date)
2019-11

(Resource Type)
journal article

(Version)
Accepted Manuscript

(URL)
https://hdl.handle.net/20.500.14094/90006463

Experimental study on interfacial and wall friction factors under counter-current flow limitation in vertical pipes with sharp-edged lower ends

Raito Goda[a], Kosuke Hayashi[a], Michio Murase[b], Shigeo Hosokawa[a], Akio Tomiyama[a*]

a Graduate School of Engineering, Kobe University, 1-1, Rokkodai, Nada, Kobe 657-8501 Japan

b Institute of Nuclear Safety System, 64 Sata Mihama-cho Mikata-gun Fukui, 919-1205 Japan

*Corresponding author: tomiyama@mech.kobe-u.ac.jp, Phone & Fax: +81-78-803-6131

A B S T R A C T

Experiments on air-water counter-current annular flows in circular vertical pipes of 20 and 40 mm in diameter were carried out to obtain databases of the interfacial and wall friction factors. The pipes were made of transparent acrylic resin to observe counter-current flow limitation (CCFL) in the pipe. The vertical pipe was connected to an upper and a lower tank. The liquid and gas phases were supplied to the upper and lower tanks, respectively. The liquid volume flow rate, the pressure gradient and the liquid volume fraction were measured to evaluate the friction factors. The flows in the pipe were observed using a high-speed video camera and the flow pattern under CCFL was identified using the time-strip visualization technique. The main conclusions obtained under the present experimental conditions are as follows: (1) the flows under CCFL condition can be classified into four regimes, i.e. the smooth film, the transition from smooth film to rough film regimes, the rough film with large amplitude disturbance waves forming at

the lower pipe end, and the rough film with simultaneous onsets of disturbance waves inside the pipe, (2) the slope of the CCFL diagram depends on the flow regimes, (3) the flow structure strongly affects the friction factors, and therefore, available correlations of friction factors not accounting for their dependences on the flow regimes cannot give good evaluations, (4) the wall friction factor can be correlated in terms only of the liquid Reynolds number, (5) the interfacial friction factor in the rough film regimes can be well correlated in terms of the gas Wallis parameter (Froude number) since the interface structure strongly depends on the Wallis parameter, and (6) the CCFL model derived using the present empirical correlations of friction factors agrees well with the CCFL characteristics data.

KEYWORDS: CCFL characteristics; Friction factors; Flow structure; Time-strip flow visualization

1. Introduction

Reflux cooling is expected as a core cooling mode during LOCA in PWR (Asaka et al., 1995). Vapor from the reactor core is condensed in U-tubes of the steam generator (SG) and the condensate returns to the core. Vapor and the condensate may form a counter current two-phase annular flow in the vertical section of the U-tube. The limitation of the falling motion of the liquid phase due to the upward gas flow is called the counter-current flow limitation (CCFL). The relationship between the flow rates of the gas phase and falling liquid is the so-called CCFL characteristics. Understanding the CCFL characteristics is therefore of great importance in evaluation of the flow rate of the condensate flowing back to the core.

Wallis (1969) proposed the following correlation of CCFL characteristics:

$$J_G^{*1/2} + m\, J_L^{*1/2} = C \tag{1}$$

where J_k^* ($k = G$ or L where G and L denote the gas and liquid phases, respectively.) are the Froude numbers or the so-called Wallis parameters defined by

$$J_k^* = J_k \Big/ \sqrt{\Delta\rho g D/\rho_k} \tag{2}$$

where J is the volumetric flux, ρ the density, g the magnitude of the acceleration of gravity, D the pipe diameter, and $\Delta\rho$ ($= \rho_L - \rho_G$) the density difference. The coefficients m and C are the slope and the intercept of the $J_L^{*1/2}$- $J_G^{*1/2}$ diagram and they depend on the pipe geometry, e.g. D, the shape of the pipe ends and so on. Many experiments on CCFL in vertical pipes have been carried out so far, and several empirical correlations of CCFL were proposed based on Eq. (1) (Clift et al., 1966; Kutateladze, 1972; Wallis et

al., 1974; Richter, 1981; Govan et al., 1991; Kaminaga et al., 1992; Jeong and No., 1996; Zapke and Kroger., 1996; Zapke and Kroger, 2000; Zapke and Kroger., 2000; Vijayan, 2001; Kusunoki et al., 2014; Kusunoki et al., 2015). In our previous study (Goda et al., 2018), we derived the fundamental functional form of a CCFL correlation, in which m and C were given in terms of the relevant dimensionless groups, from the one-dimensional momentum equations of the two-fluid model and pointed out that reliable models of the interfacial and wall friction factors, f_i and f_w, are required to improve the accuracy of the model.

Bharathan et al. (1983) carried out experiments on CCFL in a vertical pipe with sharp-edged lower end to investigate the effects of the gas flow rate on the pressure drop and the liquid volume fraction. They confirmed that at high J_G^* the liquid downward flow was fully limited, i.e. zero liquid volume flux. In this regime, the interfacial shear stress was dominant and the wall shear stress was negligibly small. They proposed a correlation of f_i, which was expressed in terms of the dimensionless liquid film thickness and the Bond number. Only the pressure drop data were used in developing the f_i correlation since the wall shear stress was neglected. On the other hand, f_w was assumed to be constant without any experimental evidence. Abe et al. (1991) numerically solved the one-dimensional momentum equations of a counter-current annular flow to obtain the interfacial and wall shear stresses. They used the experimental data of the CCFL characteristics of Bharathan et al. (1978) to close the system of equations. The f_i was correlated with a functional form similar to the Bharathan correlation. On the other hand, f_w was found to be inversely proportional to the liquid Reynolds number. The validity of the assumption of negligible wall shear stress and the applicability of the above-mentioned correlations of f_i and f_w have not

been well understood since experimental databases of CCFL are still insufficient.

The flow structure of a counter-current flow may change with the gas flow rate (Bharathan et al., 1983). The friction factors would depend on the flow structure since the behavior of interfacial waves plays an important role in friction factors. However the flow structure under CCFL has been rarely investigated.

In this study, we carried out CCFL experiments in an air-water system at atmospheric pressure and room temperature to obtain data of f_i and f_w. The liquid volumetric flux, pressure gradient and liquid volume fraction were measured to evaluate the friction factors. Vertical pipes of D = 20 and 40 mm were used to investigate the effects of D on f_i and f_w. In addition, we analyzed the flow structure in detail by using the time-strip flow visualization technique (Borhani et al., 2010).

2. Experimental

2.1 Experimental setup and measurement method

Fig. 1 shows the experimental setup, which consists of the upper tank, the circular vertical pipe (test section), the lower tank, the inlet section, the water reservoir, and the water and air supply systems. Air was supplied from the compressor to the lower tank through the regulator, the flow meter, and the pressure gauge. Water at 298 $\pm$ 5 K was supplied from the reservoir to the upper tank at the fixed volume flow rate, $Q_{L\mathrm{in}}$, of 8.3 x 10^{-5} m^3/s by using the magnet pump. Water was supplied from the upper tank to the vertical pipe and liquid film was formed on the inner wall of the pipe. Air was then flowed from the lower tank to the vertical pipe after the liquid film reached the lower tank. It should be noted that starting the air injection after the liquid film formation in the entire pipe assured that no hysteresis took place in the CCFL characteristics. Liquid

flow limitation took place due to the upward air flow, i.e. a counter-current annular flow was formed, and therefore, the flow rate of the liquid falling into the lower tank was smaller than $Q_{L\mathrm{in}}$. The J_L was measured from the temporal change in the liquid level in the lower tank. The lowest and highest J_L in the present experiments were $J_L = 4.8 \times 10^{-4} \pm 1.5 \times 10^{-5}$ m/s ($\pm$ 3.0 %) and $1.8 \times 10^{-1} \pm 5.1 \times 10^{-2}$ m/s ($\pm$ 2.9 %), respectively.

Fig. 2 (a) shows the vertical pipe for measuring the pressure gradient, dP/dz, and J_L, where P is the pressure, and z the vertical coordinate measured from the lower end of the test section. It was made of transparent acrylic resin for flow observation. The diameters, D, and the length of pipes were 40 and 20 mm, and 20D, respectively. The lower ends were sharp edged, whereas the upper ends were rounded with the radius, R, of curvature of $D/2$. The pressure difference was measured using the pressure transducer (Accuracy: $\pm$ 0.25 FS). The measurement sections were z = 20-560 and 20-280 mm for D = 40 and 20 mm, respectively. The sampling time was 1 ms and the sampling number was 50000. The measurement was repeated 36 times under each condition to assure convergence of the mean value. The uncertainties estimated at 95 % confidence in $-dP/dz$ were $\pm$ 6.1 % and $\pm$ 5.9 % at D = 40 mm and 20 mm, respectively.

Fig. 2 (b) shows the test section for measuring the liquid volume fraction, α_L. The α_L was measured by using quick closing valves (QCVs) (Funahashi et al., 2018), which consisted of two pairs of the slide plates and the air cylinders as shown in **Fig. 3**. The distances, L_c, between the QCVs were 550 and 400 mm for D = 40 and 20 mm, respectively. The QCVs were synchronized and closed within 1/30 s. Another QCV was mounted on the air supply line and was opened to prevent a sharp increase of the pressure in the lower tank when the QCVs in the test section were closed.

The liquid volume fraction, α_{Li}, of the ith measurement was obtained by measuring

the height, H_i, of the liquid in the measurement section after closing, i.e.

$$\alpha_{Li} = H_i / L_c \tag{3}$$

The ensemble-averaged volume fraction, $\overline{\alpha}_L$, was obtained as

$$\overline{\alpha}_L = \sum_{i=1}^{n} \alpha_{Li} / n \tag{4}$$

where n is the number of samples and n = 100, which was large enough to obtain well-converged values as shown in **Fig. 4**. The uncertainty estimated at 95 % confidence in $\overline{\alpha}_L$ was $\pm$ 1.1 % and $\pm$ 2.0 % for D = 40 and 20 mm, respectively.

Successive images of flows in the pipe were taken using a high-speed video camera with the frame rate 350 fps. The time-strip flow visualization technique (Borhani et al., 2010) was applied to the images, i.e. the gray values of pixels along the pipe axis were extracted from each image and rearranged in the horizontal direction as shown in **Fig. 5**. The horizontal axis of the resultant image is therefore the time. The downward motion of interfacial waves forming at a liquid film and disturbance waves moving upward due to gas flow can be clearly observed in the time-strip image.

2.2 Evaluation of interfacial and wall friction factors

The f_i and f_w are evaluated based on the one-dimensional momentum equations of a gas-liquid counter-current two-phase annular flow in a circular vertical pipe (**Fig. 6**). The flow is assumed to be steady and uniform in the streamwise direction and the single-pressure assumption is utilized. The momentum equations of the gas and liquid phases are given by

$$-\alpha_G \frac{dP}{dz} = \frac{Pe_i}{S}\tau_i + \rho_G \alpha_G g \tag{5}$$

$$-\alpha_L \frac{dP}{dz} = -\frac{Pe_i}{S}\tau_i - \frac{Pe_w}{S}\tau_w + \rho_L \alpha_L g \tag{6}$$

where α is the volume fraction and $\alpha_G + \alpha_L = 1$, Pe_i ($= \pi D \alpha_G^{1/2}$) the wetted perimeter of the gas-liquid interface, S the cross-sectional area of the pipe, τ_i the interfacial shear stress, Pe_w ($= \pi D$) the wetted perimeter of the pipe, and τ_w the wall shear stress. The τ_i and τ_w are given by

$$\tau_i = \frac{f_i}{2}\rho_G (u_G - u_L)^2 \tag{7}$$

$$\tau_w = \frac{f_w}{2}\rho_L u_L^2 \tag{8}$$

where u_L and u_G are the liquid and gas velocities, respectively, and $u = J/\alpha$. Substituting Eq. (7) into Eq. (5) yields the following expression for f_i:

$$f_i = -\frac{D\sqrt{\alpha_G}}{2\rho_G \left(J_G/\alpha_G - J_L/\alpha_L\right)^2}\left(\frac{dP}{dz} + \rho_G g\right) \tag{9}$$

By using Eqs. (7), (8) and (9), Eq. (6) can be rearranged as

$$f_w = \frac{D\alpha_L^2}{2\rho_L J_L^{\,2}}\left[\frac{dP}{dz} + \left(\alpha_G \rho_G + \alpha_L \rho_L\right) g\right] \tag{10}$$

The measured dP/dz, α, J_L and J_G were substituted into Eqs. (9) and (10) to evaluate f_i and f_w.

3. Results and discussion

3.1 CCFL characteristics and flow structure

Fig. 7 (a) shows CCFL characteristics of D = 40 mm. The $J_L^{*1/2}$ decreases with increasing $J_G^{*1/2}$. The slope, $dJ_G^{*1/2}/dJ_L^{*1/2}$, changes with $J_G^{*1/2}$. Therefore Eq. (1) with a single set of m and C cannot express the CCFL characteristics. Although we pointed out in our previous study (Goda et al., 2018) that the slope changes at about ($J_L^{*1/2}$, $J_G^{*1/2}$) = (0.1, 0.6) due to the transition between laminar and turbulent film flows, the present data show that the change in slope also takes place at lower $J_G^{*1/2}$, implying multiple flow structure changes. The CCFL characteristics at D = 20 mm shown in **Fig. 7 (b)** also changes with J_G.

Fig. 8 (a) shows an instantaneous image at D = 40 mm and ($J_L^{*1/2}$, $J_G^{*1/2}$) = (0.46, 0.37) in the J_G^* range of $0.3 < J_G^{*1/2} < 0.4$. The flow consists of the gas core and the surrounding liquid film, i.e. a counter-current annular flow is formed. The gray color in the center region represents interfacial waves at the falling liquid film. The interface structure is not disturbed so much since the gas flow rate is small. The time-strip image is shown in **Fig. 9 (a)**, where the vertical axis is z/D and t^* (= tJ_G/D) is the dimensionless time. The thin black line indicated by the arrow represents the interfacial wave moving downward with the falling liquid film. The film velocity is almost constant until reaching the lower pipe end, and the falling motion is not prevented in the pipe. This flow regime is therefore characterized by the presence of smooth films and their continuous falling motion. In the range of $0.4 \leq J_G^{*1/2} < 0.5$, disturbance waves are formed as shown in **Fig. 8 (b)** (dark colored region in the bottom part of the pipe), where ($J_L^{*1/2}$, $J_G^{*1/2}$) = (0.35, 0.44). As shown in its time-strip image (**Fig. 9 (b)**), these

disturbance waves are formed at the lower pipe end and flow upward. Some of them break down in the middle part of the pipe. The liquid phase is brought back to the upper side by the disturbance waves, and therefore, the liquid flow limitation becomes severer than the flow in **Fig. 8 (a)**. Further increase in $J_G^{*1/2}$ enhances the onset of disturbance waves as shown in **Fig. 8 (c)** (($J_L^{*1/2}$, $J_G^{*1/2}$) = (0.21, 0.53)). The time-strip image (**Fig. 9 (c)**) shows that all the disturbance waves reach the upper pipe end. Large amplitude disturbance waves are not formed in **Fig. 8 (d)** (($J_L^{*1/2}$, $J_G^{*1/2}$) = (0.03, 0.72)) since the liquid film is thin due to the strong liquid flow limitation. Disturbance waves are however simultaneously formed in the pipe as shown in the time-strip image (**Fig. 9 (d)**), whereas they do not grow larger and immediately disappear.

Bharathan et al. (1983) also carried out CCFL experiments in a vertical pipe with sharp-edged lower end and confirmed that the liquid film structure changes from smooth, transitional to rough as $J_G^{*1/2}$ increases. The flow structures in **Figs. 9 (a) and (b)** correspond to the smooth film and transitional regimes. Although Bharathan et al. (1983) classified all the flows at high $J_G^{*1/2}$ into the rough film regime, the flow structure drastically changes as shown in **Figs. 9 (c) and (d)** even in the high $J_G^{*1/2}$ range. Hereafter we will refer to the flow structures in **Figs. 9 (a), (b), (c) and (d)** as SM (smooth), TR (transitional), RF-I (rough film I) and RF-II (rough film II), respectively. The $J_G^{*1/2}$ for the flow regime transition from SM to TR ($J_G^{*1/2} \sim 0.4$) and from RF-I to RF-II ($J_G^{*1/2} \sim 0.6$) correspond to those for the change in the slope of the CCFL characteristics.

Instantaneous and time-strip images at D = 20 mm are shown in **Figs. 10 and 11**, respectively. The flow structures in **(a), (b) and (c)** can be classified into TR, RF-I and RF-II, respectively. The flow regime transition takes place at $J_G^{*1/2} \sim 0.6$, which also

corresponds to the change in the slope of the CCFL characteristics. When $J_G^{*1/2}$ was lower than the TR regime, the liquid phase filled the pipe cross section and the gas phase rose upward intermittently as shown in **Fig. 12**. The fluctuations of this oscillatory flow were not periodic and had a long time scale, so that accurate mean values could not be obtained. We will not deal with the oscillatory flow pattern in the following.

As discussed above, the time-strip images are of use to identify the flow structure and revealed that the flow structure causes the change in the slope of the CCFL characteristics. Although the flow structure transits from TR to RF-I at $J_G^{*1/2} \sim 0.5$ for D = 40 mm and 0.45 for D = 20 mm, the changes in the slopes of the CCFL characteristics are not significant. This flow regime transition however strongly affects the trends of dP/dz and α_L as will be discussed in the following section.

3.2 Pressure gradient and liquid volume fraction

Fig. 13 (a) shows α_L and the dimensionless pressure gradient, $-(dP/dz)^*$, for D = 40 mm, where $-(dP/dz)^*$ is defined by

$$-\left(\frac{dP}{dz}\right)^* = -\frac{1}{(\rho_L - \rho_G)\,g}\left(\frac{dP}{dz}\right) \tag{11}$$

In the SM regime, α_L decreases with increasing $J_G^{*1/2}$, which results in the decrease in the static pressure loss. The $-(dP/dz)^*$ is however almost constant, implying that the frictional pressure loss increases due to the increase in the fluctuation of the interface structure by the gas flow. In the TR regime, α_L and $-(dP/dz)^*$ increase with increasing $J_G^{*1/2}$. The increasing rate of the latter is especially large due to the disturbance waves forming at the lower pipe end. The α_L and $-(dP/dz)^*$ slightly decrease as $J_G^{*1/2}$ increases

in the RF-I regime. The $-(dP/dz)^*$ largely changes due to the flow regime transition although the difference in the CCFL characteristics between TR and RF-I is small as shown in **Fig. 7**. In the RF-II regime, α_L and $-(dP/dz)^*$ largely decrease since the high gas flow rate strongly prevents water from entering the pipe from the upper tank. **Fig. 13 (b)** shows the α_L and pressure gradient data of D = 20 mm. The dependences of α_L and $-(dP/dz)^*$ on $J_G^{*1/2}$ are similar to those of D = 40 mm, although the SM regime does not appear and α_L and $-(dP/dz)^*$ deviate from each other in the RF-I regime.

3.3 Interfacial and wall shear stresses

Fig. 14 (a) shows the data of τ_i and τ_w for D = 40 mm. The τ_i in the SM regime is low and almost independent of $J_G^{*1/2}$ since the interface is smooth. On the other hand, the increase in $J_G^{*1/2}$ decreases τ_w due to the decrease in the liquid flow rate. When the flow pattern changes from SM to TR, τ_i steeply increases due to the formation of disturbance waves. The disturbance waves prevent the liquid from falling down, and therefore, τ_w decreases. In the RF-I regime, τ_w is much smaller than τ_i (less than 5% of τ_i) and has negligible effects on the force balance. The α_L and $-(dP/dz)^*$ are therefore almost the same as shown in **Fig. 13 (a)**. Hence the assumption that τ_w is negligible in the rough film regime in Bharathan et al. (1983) is valid in this case. All the disturbance waves in this regime run from the lower end to the upper end. They decrease not only the liquid flow rate but also the velocity gradient in the vicinity of the pipe wall. This could be a reason of the small τ_w. In the RF-II regime, α_L is small as shown in **Fig. 13 (a)**. Therefore the amplitudes of interfacial waves are also small, resulting in the reduction of τ_i with increasing $J_G^{*1/2}$. On the other hand, τ_w slightly increases to compensate the reduction in τ_i, in other words, to balance the shear stresses with the

gravitational force:

$$\tau_i + \tau_w \cong \rho_L \delta g \tag{12}$$

where δ is the average liquid film thickness. Thus the effects of τ_w on the force balance become larger and non-negligible in RF-II.

Fig. 14 (b) shows τ_i and τ_w for D = 20 mm. The dependences of τ_i and τ_w on $J_G^{*1/2}$ are similar to those for D = 40 mm. However τ_w is about 20% of τ_i, resulting in non-negligible effects of τ_w and the large difference between α_L and $-(dP/dz)^*$ shown in **Fig. 13 (b)**. The Bharathan's assumption is not valid in this case, and therefore, its validity depends not only on the flow structure but also on D. Although they proposed the f_i correlation by neglecting τ_w, the τ_w effects in f_i should be taken into account to develop more reliable correlations.

3.4 Wall friction factor

Fig. 15 shows the wall friction factor f_w. The f_w decreases with increasing the liquid Reynolds number, Re_L, defined by

$$Re_L = \frac{\rho_L J_L D}{\mu_L} \tag{13}$$

where μ_L is the liquid viscosity. The data in the RF regimes are independent of D. The following f_w correlation for co-current annular flows, which has often been even used for CCFL predictions due to the lack of f_w correlations for counter-current flows, is compared with the data:

$$f_w = \begin{cases} \dfrac{16}{Re_L} & : \text{for laminar flows } (Re_L \leq 2000) \\ \dfrac{0.079}{Re_L^{1/4}} & : \text{for turbulent flows } (Re_L > 2000) \end{cases} \quad (14)$$

The data under the turbulent flow condition agree with Eq. (14), whereas, in the laminar flows, the slope of f_w is much larger than Eq. (14), implying that the velocity gradient at the pipe wall is steeper than that in the co-current flow model. Abe et al. (1991) numerically predicted the velocity profile in a liquid film by making use of Bharathan's CCFL characteristics data and also pointed out that the velocity gradient at the wall would be large. They proposed the following empirical correlation by accounting for this fact:

$$f_w = \frac{300}{Re_L} \quad (15)$$

Eq. (15) is compared with the present data in the figure. This correlation gives evaluations much better than Eq. (14) at $Re_L \sim 100$ in the RF regime. Its slope is however smaller than the data and the deviation becomes larger as Re_L is apart from $Re_L \sim 100$ in the RF regime.

The following function well represents the present data in the RF regimes as shown in the figure (dashed line):

$$f_w = \frac{2.86 \times 10^4}{Re_L^{1.96}} \quad (16)$$

3.5 Interfacial friction factor

Fig. 16 shows f_i. The f_i increases with increasing α_L in the RF regimes, and f_i of D =

40 mm is larger than that of D = 20 mm. Therefore f_i cannot be correlated in terms only with α_L. In the SM and TR regimes, the dependence of f_i on α_L is much more complicated.

The following f_i correlation for co-current annular flows proposed by Wallis (1969) underestimates the data:

$$f_i = 0.005(1 + 75\alpha_L) \tag{17}$$

Bharathan et al. (1983) proposed the following f_i correlation for the rough film regime, which accounts for the effects of D:

$$f_i = 0.005 + A\delta^{*B} \tag{18}$$

where δ^* is the dimensionless liquid film thickness defined by

$$\delta^* = \frac{\delta}{\sqrt{\sigma/(\rho_L - \rho_G)g}} \tag{19}$$

where σ is the surface tension. Using the dimensionless pipe diameter, $D^* = D/\sqrt{\sigma/(\rho_L - \rho_G)g}$, δ^* can also be expressed as $\delta^* = (1 - \sqrt{\alpha_G})\, D^*/2$. The A and B in Eq. (18) are functions of D^* given by

$$\log_{10} A = -0.56 + 9.07/D^* \tag{20}$$

$$B = 1.63 + 4.74/D^* \tag{21}$$

Eq. (18) is plotted for D = 40 and 20 mm. Although Eq. (18) was developed by neglecting τ_w, f_i evaluated using Eq. (18) coincidentally agrees with the data in RF-II of D = 40 mm. The evaluations however largely deviate from the data in RF-I. In addition the D effect in Eq. (18) becomes smaller and smaller as α_L increases, whereas the data

show strong effect of D even at high α_L.

Due to the high gas flow rate and the wavy structure of the film interface, the form drag would be dominant in f_i. This is supported by the fact that f_i cannot be well correlated in terms of the Reynolds number, which accounts for the viscous effect, as shown in **Fig. 17**. Eq. (17) accounts for this fact by using the constant, 0.005, and α_L as the parameter taking into account the interface roughness based on the analogy to the single-phase flow in a rough wall pipe. This correlation, however, cannot give good evaluations. Under CCFL conditions, the gravitational force would play an important role in the interface structure since the liquid phase falls downward oppositely to the upward motion of the gas phase. The f_i is therefore plotted in **Fig. 18** against $J_G^{*1/2}$, which is the ratio of the inertial force to the gravitational force. The data in the RF regimes are well correlated in terms of $J_G^{*1/2}$, and the following correlation,

$$f_i = \begin{cases} 0.11 J_G^{*-1.98} D^{*0.43} \alpha_L & \text{in RF - I regime} \\ 0.11 J_G^{*-1.96} D^{*0.42} \alpha_L & \text{in RF - II regime} \end{cases} \tag{22}$$

agrees well with present data as shown in **Fig. 19**. The f_i data in the TR regime, however, show some dependence on D. Accumulating more data of f_i in SM and TR is necessary to model f_i in these regimes.

In our previous study (Goda et al., 2018), we derived the following fundamental form of CCFL characteristics correlation from the one-dimensional momentum equations:

$$\left(\frac{2a'}{N_G^{b'}}\right)^{\frac{1}{4}} J_G^{*\frac{1}{2}-\frac{b'}{4}} + \left(\frac{2a}{N_L^{b}}\right)^{\frac{1}{4}} J_L^{*\frac{1}{2}-\frac{b}{4}} = const. \tag{23}$$

where N_k is the inverse viscosity number of the phase k defined by

$$N_k = \frac{\sqrt{\rho_k(\rho_L - \rho_G)gD^3}}{\mu_k} \tag{24}$$

The functional form of f_w and f_i were assumed as

$$f_w = \frac{a}{Re_L^b} \tag{25}$$

$$f_i = \frac{a'}{Re_L^{b'}}\alpha_L \tag{26}$$

where a, b, a' and b' are constants. For the present CCFL in the RF regimes, Eq. (16) can be used for f_w. Hence a = 2.86 x 10^4 and b = 1.96. Submitting the functional form, $f_i = a' J_G^{*-b'} D^{*c}\alpha_L$ into the one-dimensional momentum equations, instead of Eq. (26), yields

$$\left(2a' D^{*c}\right)^{\frac{1}{4}} J_G^{*\frac{1}{2}-\frac{b'}{4}} + \left(\frac{2a}{N_L^b}\right)^{\frac{1}{4}} J_L^{*\frac{1}{2}-\frac{b}{4}} = \gamma \tag{27}$$

where the constants a', b' and c are given in Eq. (22) and $\gamma = 1$, which was determined by fitting the functional form to the data. **Fig. 20** shows comparisons between Eq. (27) and the data. The CCFL model with the empirical correlations of f_i and f_w agrees well with the data.

Fig. 20 shows comparisons between Eq. (27) and the data. The CCFL model with the empirical correlations of f_i and f_w agrees well with the data. The CCFL model also gives good evaluations for the CCFL data of Kusunoki et al. (2015) as shown in **Fig. 21** even though the pipe length, 500 mm, in their experiment is different from the present one, 400 mm.

4. Conclusion

Experiments on air-water counter-current annular flows in circular vertical pipes of 20 and 40 mm in diameter with sharp-edged lower ends were carried out to investigate the flow structure and the interfacial and wall friction factors. The pipes were made of transparent acrylic resin to observe counter-current flow limitation (CCFL). The liquid flow rate, the pressure gradient and the liquid volume fraction were measured to evaluate the friction factors. The time-strip flow visualization was carried out to understand the flow structure in detail. The main conclusions obtained under the present experimental conditions are as follows:

(1) The flows under CCFL condition can be classified into four regimes, i.e. the smooth film (SM), the transition (TR) from SM to rough film regimes, the rough film with large amplitude disturbance waves forming at the lower pipe end (RF-I), and the rough film with simultaneous onsets of disturbance waves inside the pipe (RF-II).

(2) The slope of the CCFL diagram depends on the flow regimes.

(3) The flow structure strongly affects the friction factors, and therefore, available correlations of friction factors not accounting for their dependences on the flow regimes cannot give good evaluations.

(4) The wall friction factor can be correlated in terms of the liquid Reynolds number.

(5) The interfacial friction factor in the RF regimes can be well correlated in terms of $J_G^{*1/2}$ (Froude number) since the interface structure strongly depends on $J_G^{*1/2}$.

(6) The CCFL model derived using the present empirical correlations of f_i and f_w agrees well with the CCFL characteristics data.

Acknowledgement

The authors would like to express their thanks to Mr. Takeyuki Shimamura for his assistance in the experiments.

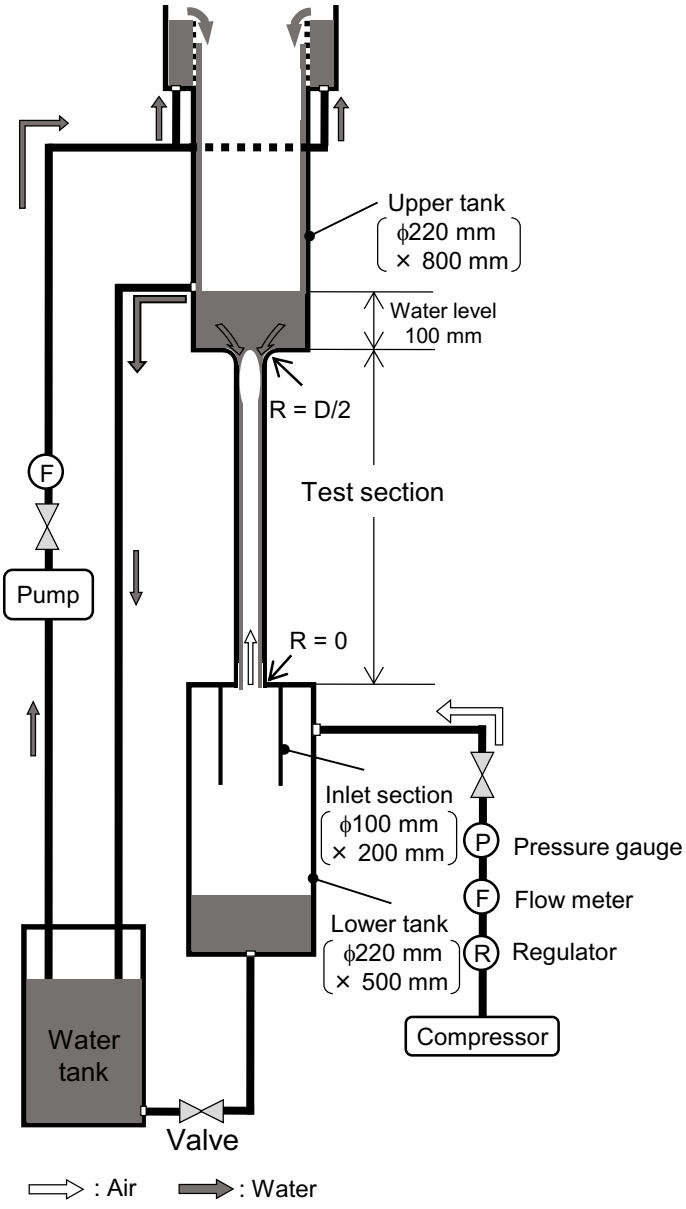

Fig. 1 Experimental setup

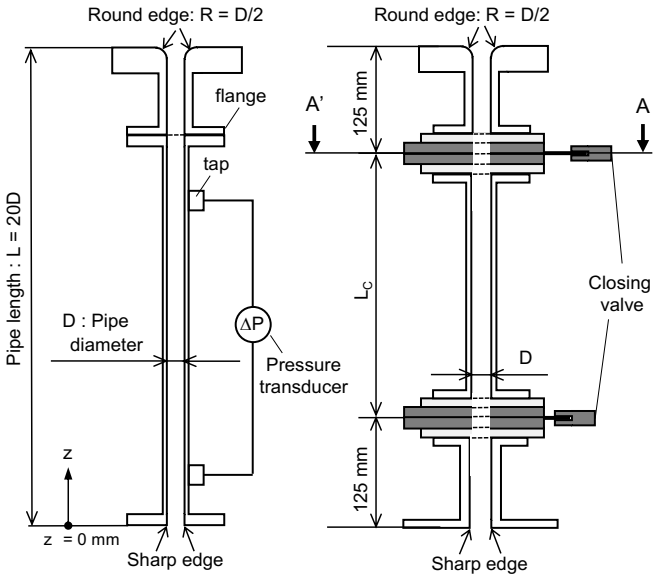

(a) Type A (b) Type B

Fig. 2 Vertical pipes of test sections (D = 20 or 40 mm)

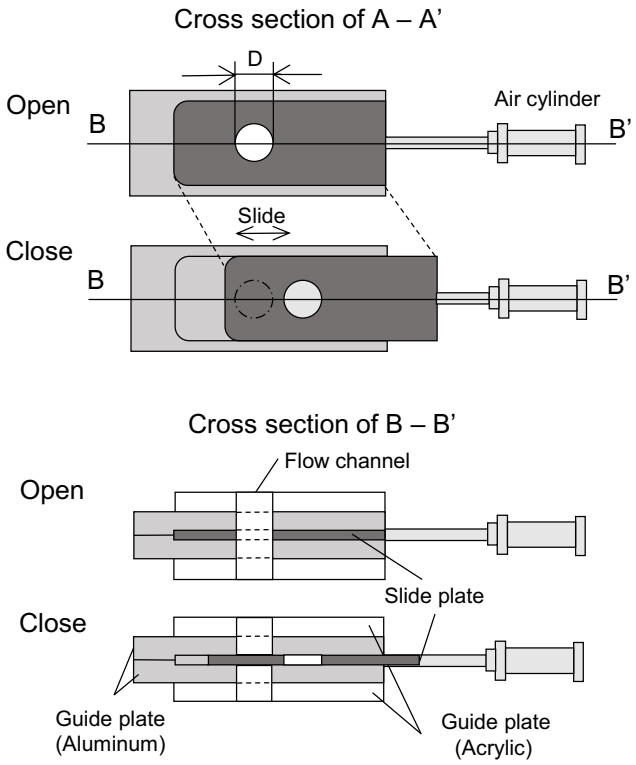

Fig. 3 Quick closing valve

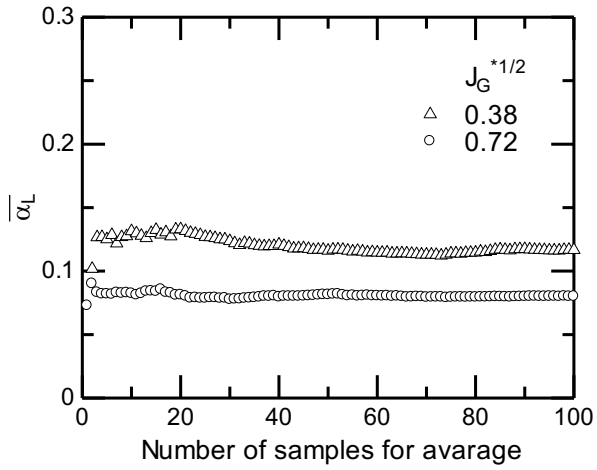

Fig. 4 Convergence of $\overline{\alpha_L}$

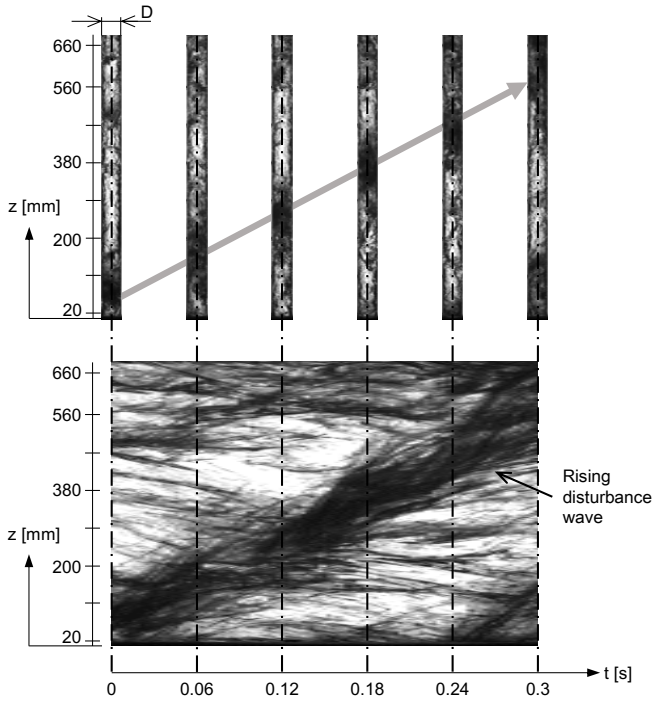

Fig. 5 Time-strip visualization technique (Top: raw images, Bottom: time-strip image)

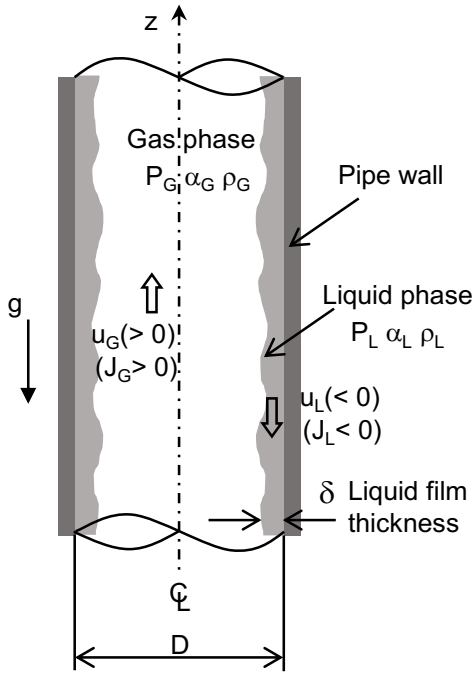

Fig. 6 Annular flow model for counter-current flow

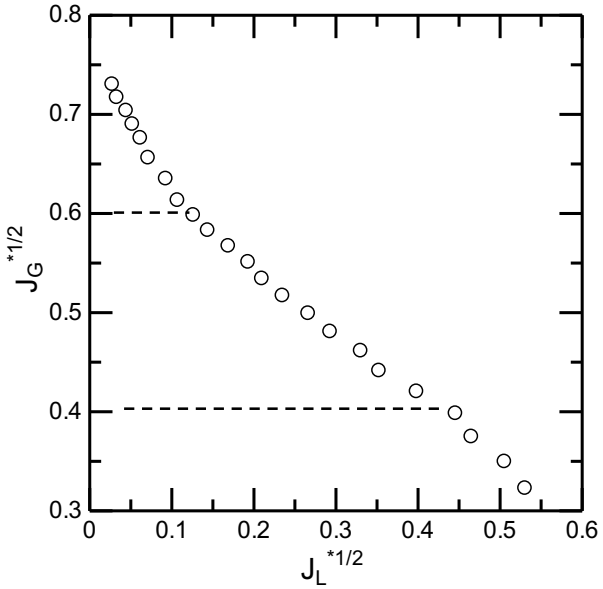

(a) $D = 40$ mm

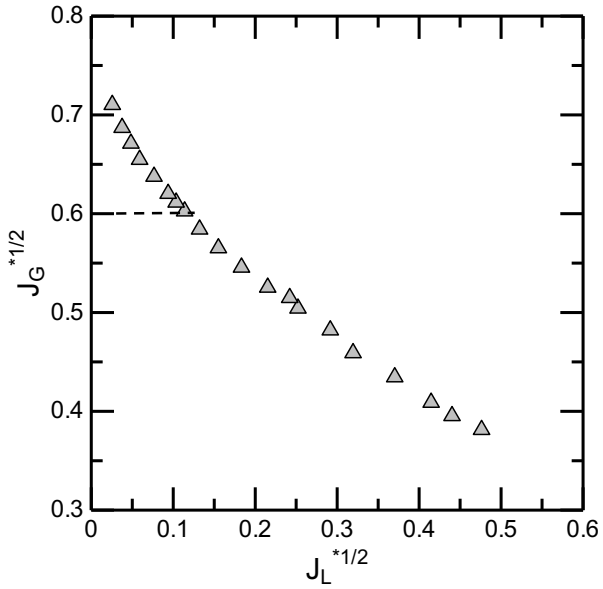

(b) $D = 20$ mm

Fig. 7 CCFL characteristics

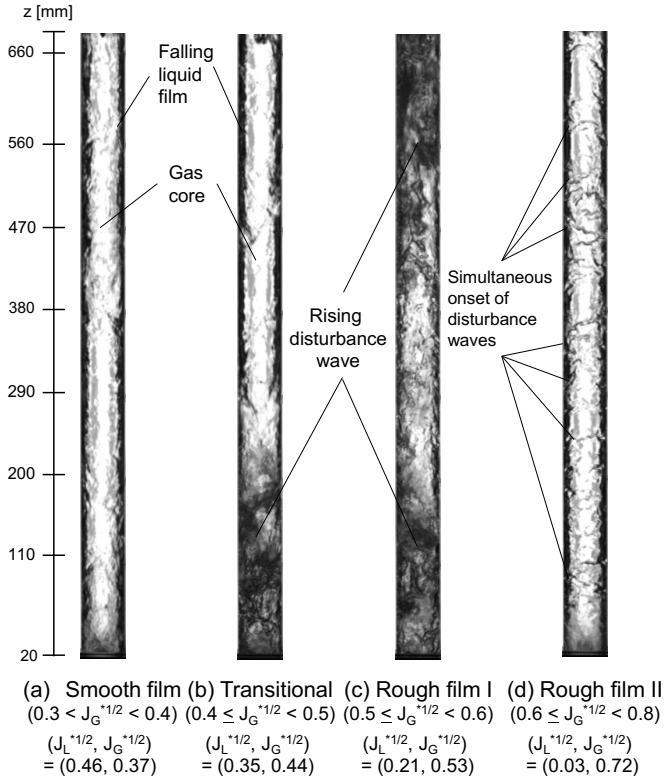

Fig. 8 Instantaneous images (D = 40 mm)

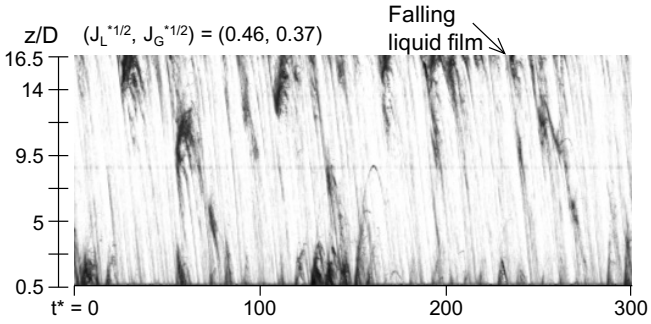

(a) Smooth film ($0.3 < J_G^{*1/2} < 0.4$)

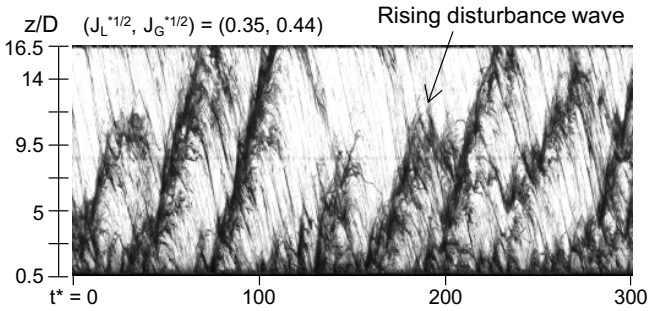

(b) Transitional ($0.4 \leq J_G^{*1/2} < 0.5$)

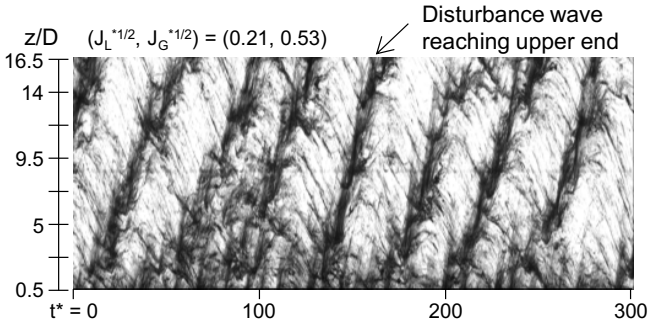

(c) Rough film I ($0.5 \leq J_G^{*1/2} < 0.6$)

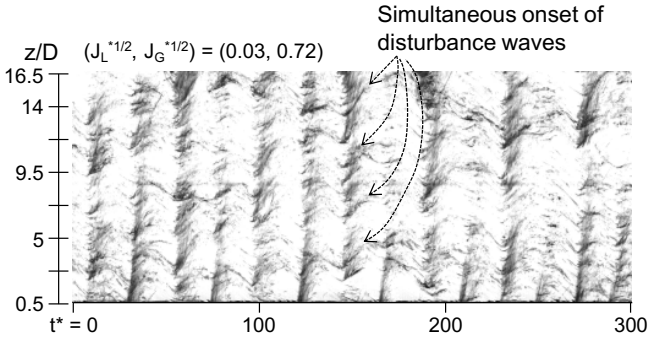

(d) Rough film II ($0.6 \leq J_G^{*1/2} < 0.8$)

Fig. 9 Time-strip images ($D = 40$ mm) ($t^* = tJ_G / D$)

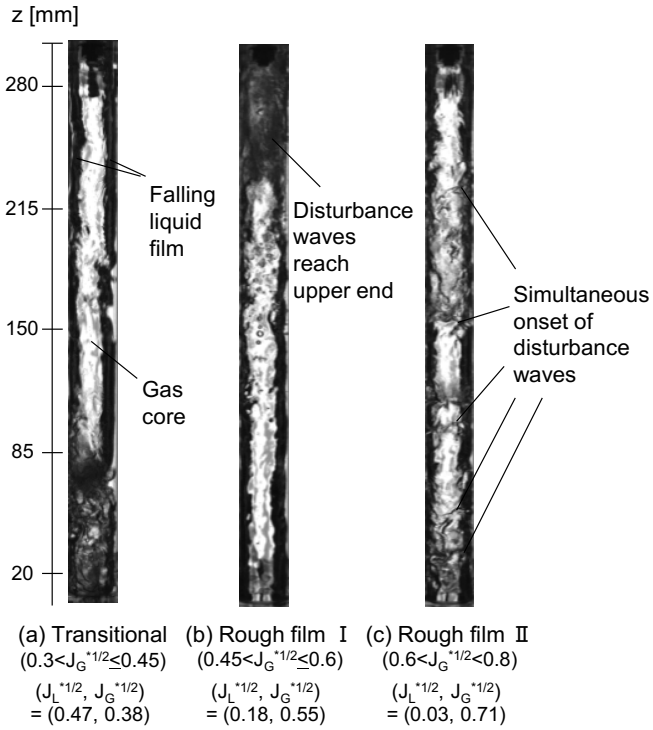

Fig. 10 Instantaneous images (D = 20 mm)

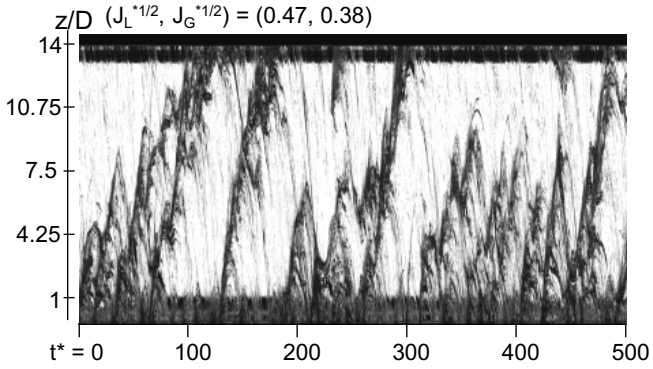

(a) Transitional ($0.3 \leq J_G^{*1/2} < 0.45$)

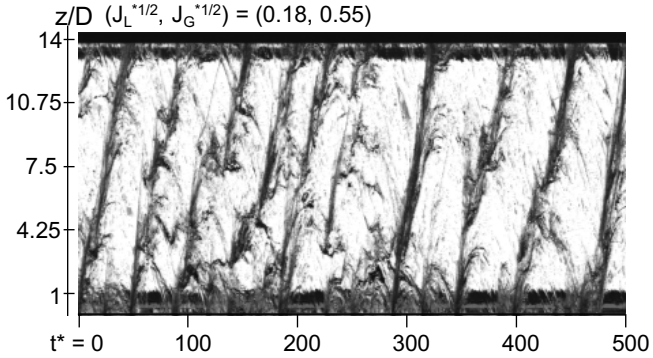

(b) Rough film I ($0.45 \leq J_G^{*1/2} < 0.6$)

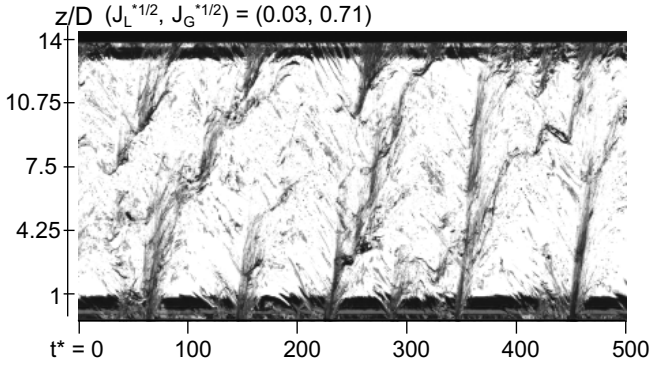

(c) Rough film II ($0.6 \leq J_G^{*1/2} < 0.8$)

Fig. 11 Time-strip images (D = 20 mm) ($t^* = tJ_G / D$)

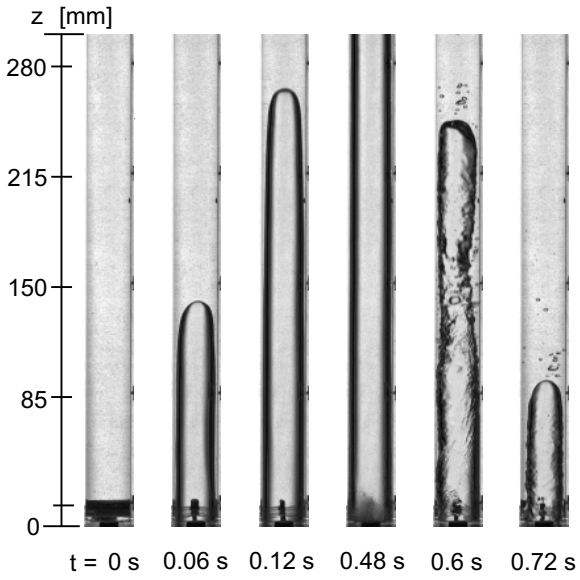

Fig. 12 Intermittent flow at low J_G (J_G =1.7 m/s and D = 20 mm)

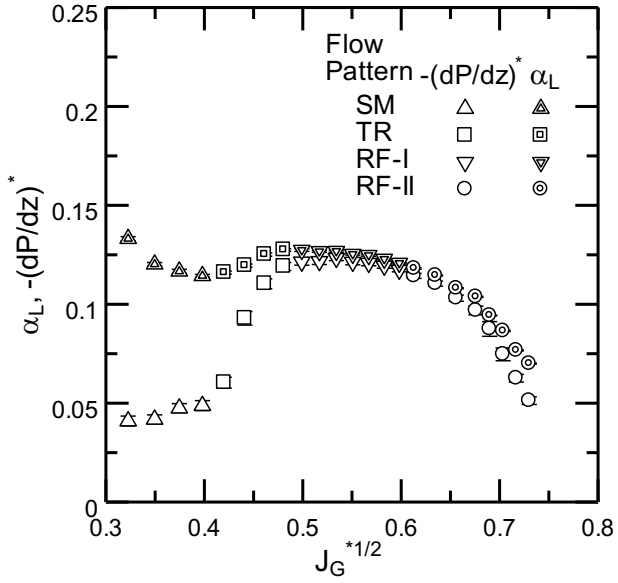

(a) $D = 40$ mm

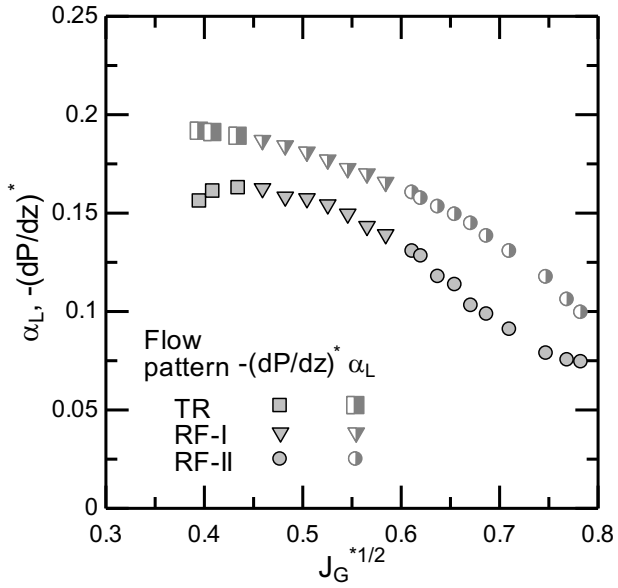

(b) $D = 20$ mm

Fig. 13 Liquid volume fraction, α_L, and dimensionless pressure gradient, $-(dP/dz)^*$

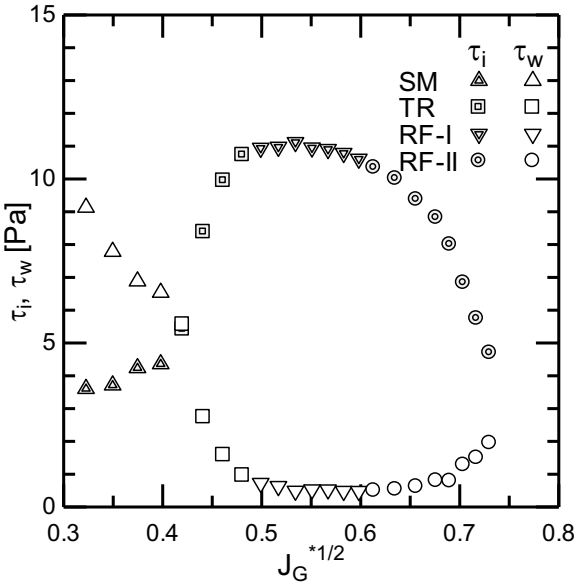

(a) $D = 40$ mm

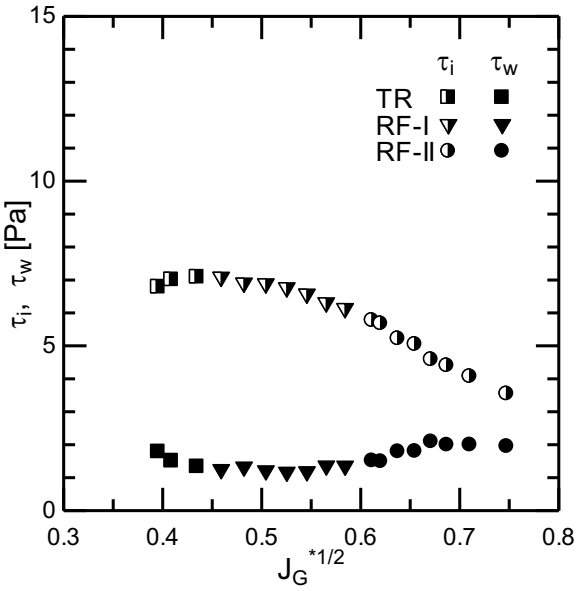

(b) $D = 20$ mm

Fig. 14 Interfacial and wall shear stresses

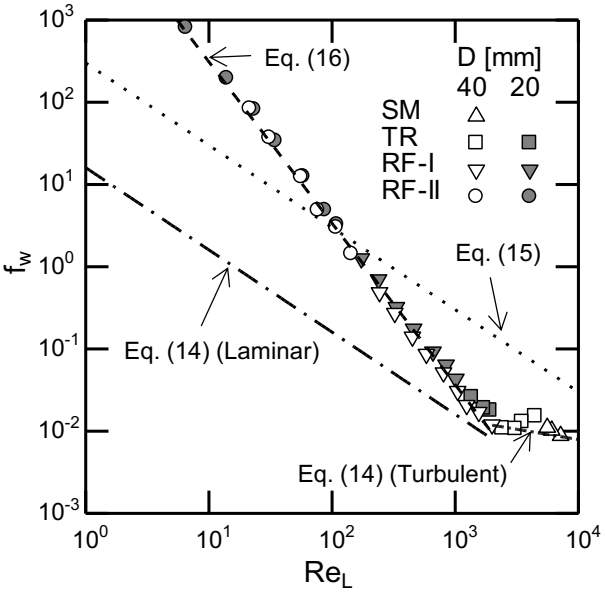

Fig. 15 Wall friction factor

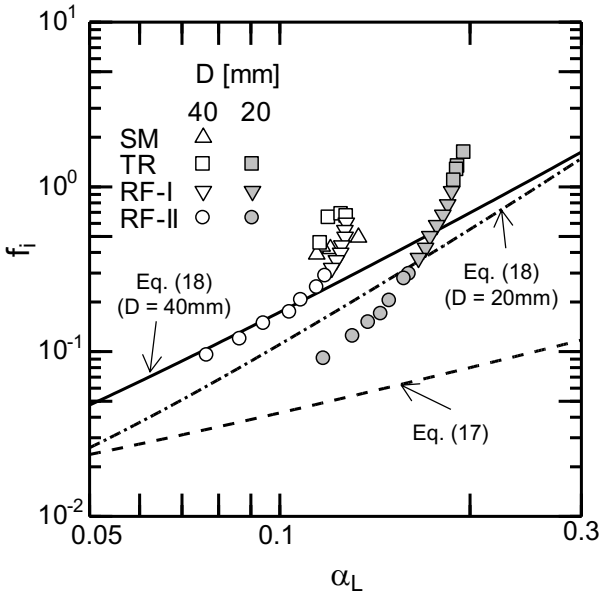

Fig. 16 Interfacial friction factor

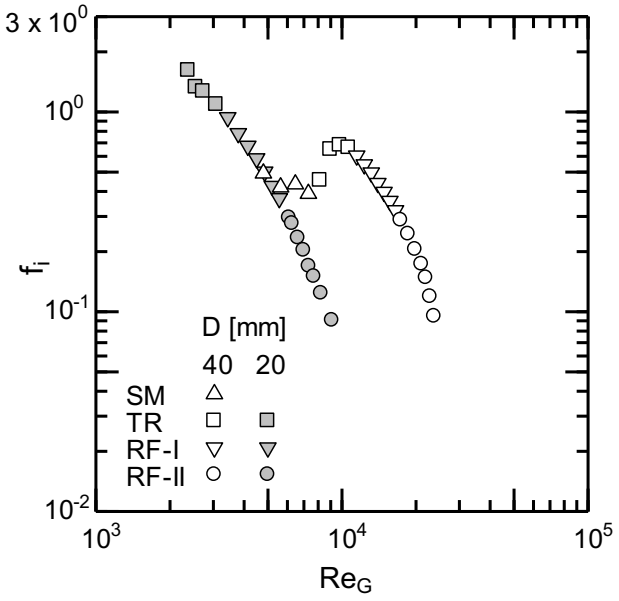

Fig. 17 Interfacial friction factor vs. Re_G

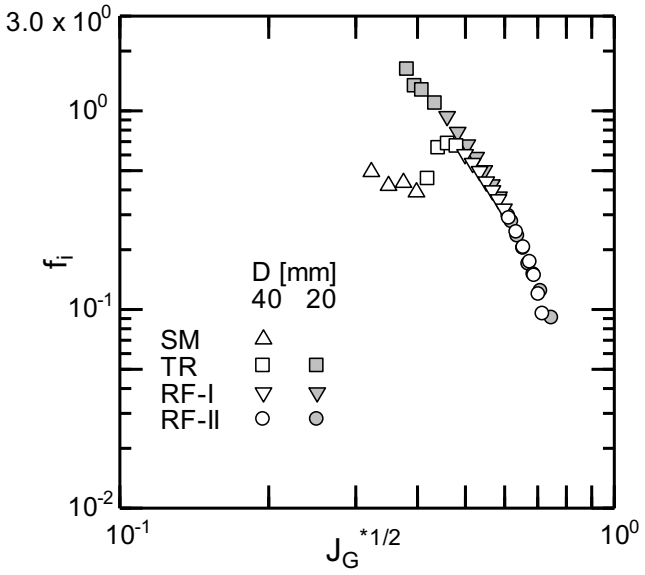

Fig. 18 Interfacial friction factor vs. $J_G^{*1/2}$

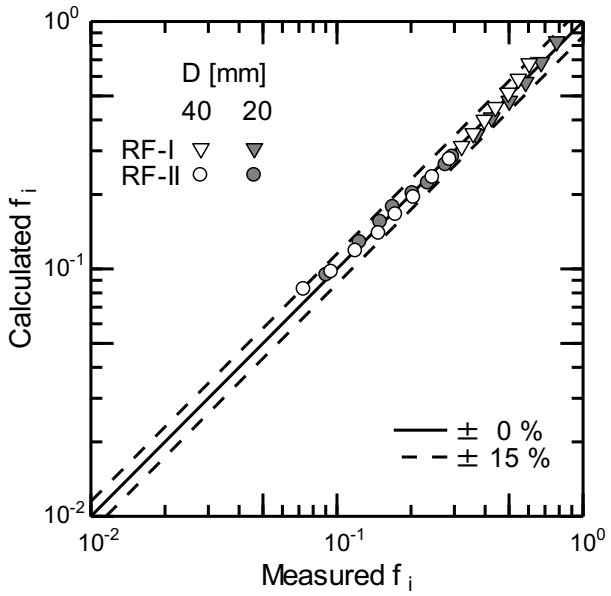

Fig. 19 Comparisons between Eq. (22) and f_i data in RF regimes

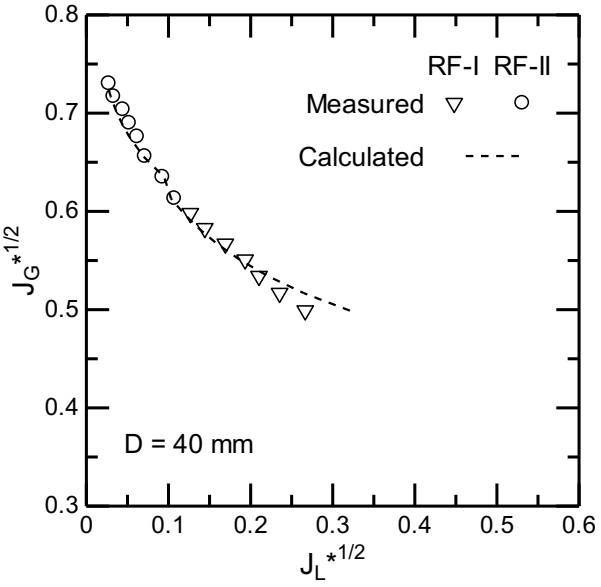

(a) $D = 40$ mm

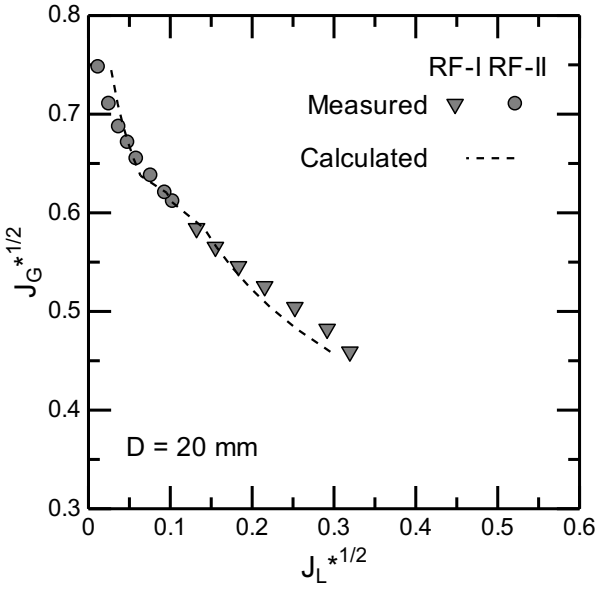

(b) $D = 20$ mm

Fig. 20 Comparisons of CCFL characteristics between data in RF regimes and Eq. (27)

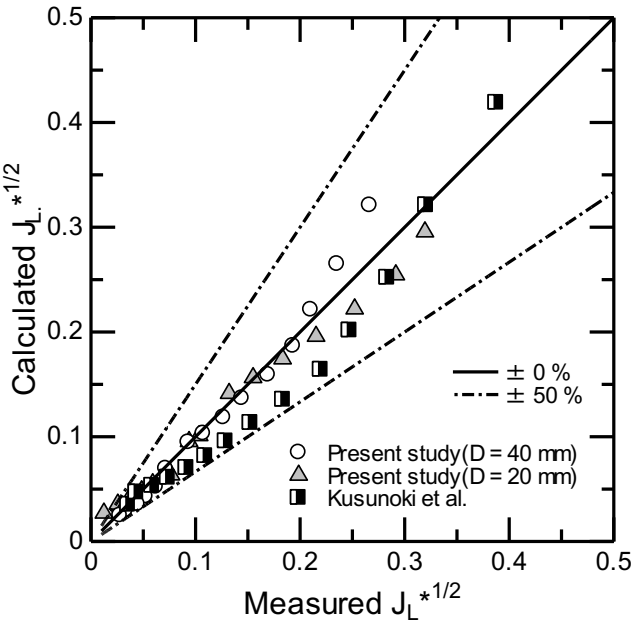

Fig. 21 Comparisons between CCFL model, Eq. (27) with Eqs. (16) and (22), and CCFL data